

# From 3D Magnetic Resonance Images to Structural Representations of the Cortex Topography using Topology Preserving Deformations

**JEAN-FRANÇOIS MANGIN**

*mangin@uriens.shfj.cea.fr*  
*Service Hospitalier Frédéric Joliot, Commissariat à l'Énergie Atomique, 91401 Orsay Cedex, France*  
*Département Images, École Nationale Supérieure des Télécommunications, 75634 Paris Cedex 13, France*

**VINCENT FROUIN**

*frouin@uriens.shfj.cea.fr*  
*Service Hospitalier Frédéric Joliot, Commissariat à l'Énergie Atomique, 91401 Orsay Cedex, France*

**ISABELLE BLOCH**

*bloch@ima.enst.fr*  
*Département Images, École Nationale Supérieure des Télécommunications, 75634 Paris Cedex 13, France*

**JEAN RÉGIS**

*Service de Neurochirurgie Fonctionnelle et Stéréotaxique, C.H.U. La Timone, 13005 Marseille, France*

**JAIME LÓPEZ-KRAHE**

*lopez@ima.enst.fr*  
*Département Images, École Nationale Supérieure des Télécommunications, 75634 Paris Cedex 13, France*

Received ?? . Revised ??.

**Abstract.** We propose an algorithm allowing the construction of a structural representation of the cortical topography from a T1-weighted 3D MR image. This representation is an attributed relational graph (ARG) inferred from the 3D skeleton of the object made up of the union of gray matter and cerebrospinal fluid enclosed in the brain hull. In order to increase the robustness of the skeletonization, topological and regularization constraints are included in the segmentation process using an original method: the homotopically deformable regions. This method is halfway between deformable contour and Markovian segmentation approaches. The 3D skeleton is segmented in simple surfaces (*SS*s) constituting the ARG nodes (mainly cortical folds). The ARG relations are of two types: first, the *SS* pairs connected in the skeleton; second, the *SS* pairs delimiting a gyrus. The described algorithm has been developed in the frame of a project aiming at the automatic detection and recognition of the main cortical sulci. Indeed, the ARG is a synthetic representation of all the information required by the sulcus identification. This project will contribute to the development of new methodologies for human brain functional mapping and neurosurgery operation planning.

**Keywords:** medical imaging, mathematical morphology, deformable contour, Markovian random fields, topology preserving deformation, structural pattern recognition, functional brain mapping

## 1. Introduction

The analysis of cerebral functional data, obtained for instance from positron emission tomography (PET) or magneto-encephalography (MEG), often requires complementary anatomical informa-

tion obtained from magnetic resonance imaging (MRI). A number of intra-individual cross-modality registration methods have been proposed for this purpose [1]. Hence, in order to proceed further with functional data analysis, various anatomical structures have to be identified in the

MR image. The unambiguous identification of internal structures like caudate or thalamus nuclei is possible in high resolution MR images, when the neuro-anatomist is guided by a reference atlas [2], thanks to a relatively low inter-individual anatomical variability. In return, it appears much more difficult to overcome the variability of the highly convoluted human cortex. Indeed, the few studies dealing with this variability are only descriptive [3] and therefore give no real methodology to identify cortical structures.

The cortex is a thin highly convoluted layer of neurons located at the brain external surface level. With respect to the MR image resolution, the cortex is constituted of gray matter located between cerebro-spinal fluid (CSF) and white matter (see Fig. 1). This gray matter layer includes numerous folds, which are deep narrow fissures in the brain that increase the cortical surface size.

This paper describes a part of a project aiming at the automatic detection and recognition of the main cortical sulci. In this paper, the term sulcus denotes an anatomical entity which can include several folds according to individuals (a sulcus made up of several folds is an interrupted sulcus). Such tools would be an important contribution to the design of new methodologies for the human brain functional mapping, because they would allow accurate comparative studies across individuals [4]. Other applications are foreseeable in neurosurgery for operation planning which minimizes the risks of heavy functional after effects (for instance, 3D visualizations of sulci have allowed us to utilize natural sulcal pathways to gain access to pathologic structures within the brain, while preserving the integrity of healthy adjacent tissues). This paper focuses on the first of the three parts of our project, which are:

1. The design of a robust method allowing the extraction of a structural representation of the cortex topography from a T1-weighted 3-D MR image.
2. The constitution of a large database of such cortex representations in which the main sulci are identified [5], [6], [7].
3. The elaboration of a generic structural model of the cortex topography from this database and the design of a method matching this

model and any individual cortex representation [7], [8], [9], [10].

The human cortex is a subject of increasing interest in the image processing domain. Several approaches have been proposed recently in order to interpret the cortex topography from 3D MR images. Some of them rely on 2D representations: for each brain hemisphere, the distance between the brain surface and the hemisphere convex hull projected on an ellipsoid [11]; one-to-one correspondence between the brain surface and a parameterized surface obtained by “surface flattening” [4]; 2D skeleton of the folds inscribed on the brain surface [12]. Other attempts focus on 3D representations: crest lines of the brain [13] (which appears particularly difficult to manage considering the complexity of the cortex convolutions) or a 3D medial manifold of a brain negative mold [14]. Our approach relies on a 3D skeleton, which overcomes the limits inherent to 2D representations and to the high complexity of a 3D medial manifold for further processing.

The rest of this paper is organized in four sections. Section 2 describes briefly why conventional segmentation methods are ill-adapted to the robust detection of cortical folds. Section 3 proposes first a clarification of the notion of topological equivalence between 3D binary images. Then the main outlines of a new segmentation method based on topology preserving deformations are introduced. Section 4 describes the application of this method to the segmentation of the object constituted by the union of gray matter and CSF (see Fig. 1). Last section addresses the construction of an attributed relational graph (ARG) inferred from the 3D skeleton of this object. The ARG nodes are mainly cortex folds (or sulcus parts) and the ARG relations are of two types: first, pairs of folds topologically connected; second, pairs of folds delimiting a gyrus (cortical structures dual to the sulci). This high level synthetic structure provides a powerful way of dealing with anatomical variability (location, size, depth and orientation of sulci, sulcus relationships...) during the sulcus recognition tasks.

## 2. Detection of cortical folds

A structure representing the cortex topography has to take into account the numerous cortical

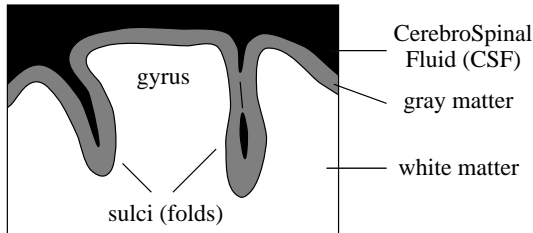


Fig. 1. Interfaces delimiting the cerebral cortex. The “CSF/ gray matter” interface can turn out to be difficult to detect when cortical folds are narrow with respect to resolution, because of partial volume effect. In return, the similar problem rarely occurs with the “CSF/ white matter” interface because gyrus white matter has a minimal thickness larger than resolution.

folds. It should be noted that the cortical parts delimited by sulci, namely the gyri, are relatively ill-defined from a morphological point of view which prevents their direct detection. Nevertheless, the notion of gyrus is of great importance when dealing with brain functions because it leads to a cortex parcellation which can be viewed as a map transposable between individuals. Consequently, we intend to develop in the future mathematical tools allowing transformation from our sulcus based representation to a gyrus based map.

In order to get 3D representations of cortical folds, two morphological approaches seem possible:

1. The detection of the “CSF/ gray matter” interface, each fold is then an excrescence of the CSF region in the brain.
2. The detection of the “gray matter/white matter” interface, each fold is then an excrescence of the {CSF, gray matter} union in the brain.

Skeletonization is a powerful way of detecting excrescences of an object, but such an approach has to be used cautiously because thinning algorithms are very sensitive to noise. A number of methods for brain segmentation or brain tissue labelling have been proposed in the literature [15], [16], [17], [18]. Since these methods generally focus on visualization or classification applications, they are not really concerned with the topology of segmented objects. In return, in order to make the fold detection rely on a 3D skeletonization, we have to assure that the segmented object has the topology of the real object (namely, without considering ventricles and internal nu-

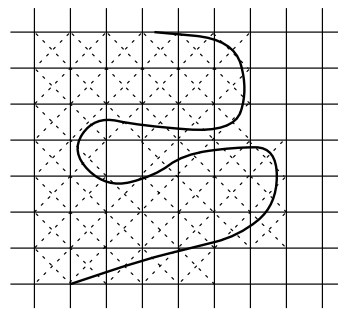


Fig. 2. The discretization of a deformable contour can cause topological modifications (a cavity creation in the figure). It should be noted that the simplicity of the discretization algorithm used in this figure is not concerned. Indeed, the only way to prevent that kind of phenomena would be the introduction of global topological constraints in the discretization algorithm.

clei made up of gray matter, the topology of a solid ball will one cavity). With respect to this constraint, the first detection approach proposed above appears difficult to perform because of partial volume effect (see Fig. 1). Therefore, we have chosen the second one.

Several attempts have been made to detect the “gray matter/white matter” interface using deformable contours. In fact, conventional deformable contours turn out to be particularly ill-adapted to this problem:

- First, with respect to image resolution, this interface includes  $C^1$  discontinuities incompatible with conventional regularization terms [19], [20]. Attempts to overcome this difficulty using additional pressure-like external forces have not been successful up to now [21]. An oversampling of the deformable contour could solve the problem but would be especially expensive in 3D. Adaptive deformable models could also be a solution [22].
- Second, because of the cortical fold narrowness, a deformable contour may cross itself and loose its topology.
- Third, edge detectors used to construct attraction forces driving the deformable contour give bad results in cortical folds because of the presence of four interfaces close to each other (see Fig. 1).
- Last, with regard to our specific requirements, since we want to perform a skeletonization, the deformable contour has to be discretized after the detection. Unfortunately, such a discretiza-

tion can induce topological modifications (see Fig. 2). This difficulty would be overcome if the fold detection was relying on brain surface or “gray matter/white matter” interface crest lines [13]. In return, with regard to the numerous convolutions of these surfaces, selection of relevant crest lines from the result of standard detection algorithms may turn out to be difficult.

Considering all these difficulties, we have developed a new segmentation approach allowing us to impose both the result topology and a smooth result interface including potential  $C^1$  discontinuities. Hence, the following skeletonization step is not disturbed by topological noise (cavities, “tunnels”) or noisy frontiers.

### 3. Topology preserving deformations

In this section, we describe the main theoretical ideas from which is constructed our segmentation method. This method relies on topology preserving deformations aiming at minimizing an energy of the form of a Gibbs distribution Hamiltonian. Hence this approach is halfway between deformable contour and Markovian segmentation approaches. Topological properties are imposed to an initial binary image which is deformed in order to reach an energetic goal. Therefore this method can be viewed as a topological regularization approach.

#### 3.1. Topological equivalence

This subsection intends to provide the reader with a parallel between classical definitions of topological equivalence in continuous spaces and recent definitions proposed for 3D binary images. The goal is not the proposition of new topological results, but first a clarification of what topology preservation can mean for 3D binary images (in fact no real consensus exists on this notion), second the derivation of a definition of topology preserving deformations appropriate to our segmentation purpose. Since this clarification is aimed at the image analysis community, it is written to be as far as possible mathematically self-contained.

**Continuous spaces** With regard to objects (or subspaces) embedded in  $\mathbb{R}^3$ , a lot of levels of topological equivalence can be proposed. Let us consider a few ones based on the following definitions of equivalence (for the sake of clarity, the definitions of standard topological notions like homeomorphism, deformation, deformable retract, homotopy type or isotopy type are regrouped in appendix A):

REL. 1  $X$  and  $Y$  share the same homotopy type.

REL. 2 There exists a homeomorphism between  $X$  and  $Y$  (implies Rel. 1).

REL. 3 There exists a finite sequence of objects  $X = X_0, X_1, \dots, X_n = Y$  such that using Def. A.18 it can be proved simultaneously, first that  $X$  and  $Y$  share the same homotopy type, and second, using the sequence of complements  $\mathbb{R}^3 - X_0, \mathbb{R}^3 - X_1, \dots, \mathbb{R}^3 - X_n$ , that  $\mathbb{R}^3 - X$  and  $\mathbb{R}^3 - Y$  share the same homotopy type (implies Rel.1).

REL. 4 There exists a deformation  $\{h_t\}$  of  $\mathbb{R}^3$  such that  $h_1 X = Y$  [23].

REL. 5 There exists a homeomorphism of  $\mathbb{R}^3$  onto itself which maps  $X$  onto  $Y$  (implies Rel. 1, 2, and 3).

REL. 6  $X$  and  $Y$  share the same isotopy type (implies Rel. 1, 2, 3, 4 and 5).

These equivalence relations differ mainly for three reasons:

1. Looseness of the two first relations relatively to the following ones results from the fact that they do not take into account the way in which objects are embedded in the surrounding space. Note particularly that the property of being knotted is not an intrinsic topological property of objects and hence is not discerned by these relations (see Fig. 3).
2. Another important distinction can be made between relations involving homeomorphisms (2, 5, 6) and other ones (1, 3, 4). Indeed, since the local dimension for any object (or background) point is the same as that of its image under a homeomorphism [24], homeomorphisms result in more stringent relations (see Fig. 4).

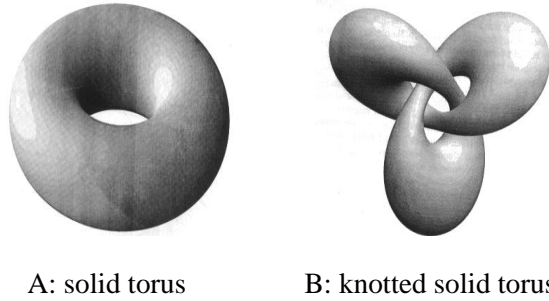


Fig. 3. Two homeomorphic objects (their fundamental groups (see section 3.1) are isomorphic to  $\mathbb{Z}$ ) which are not equivalent for Rel. 3, 4, 5 and 6 because they are differently embedded in space. Complements in  $\mathbb{R}^3$  do not share the same homotopy type (fundamental group of the left object complement is isomorphic to  $\mathbb{Z}$  while that of the right object is isomorphic to fundamental group of clover-leaf (or trefoil) knot which presentation would require an introduction to knot theory [25]). It should be noted that in opposition to right object, some objects are endowed with more intricate fundamental group than their complements (see Fig. 3 of [23]).

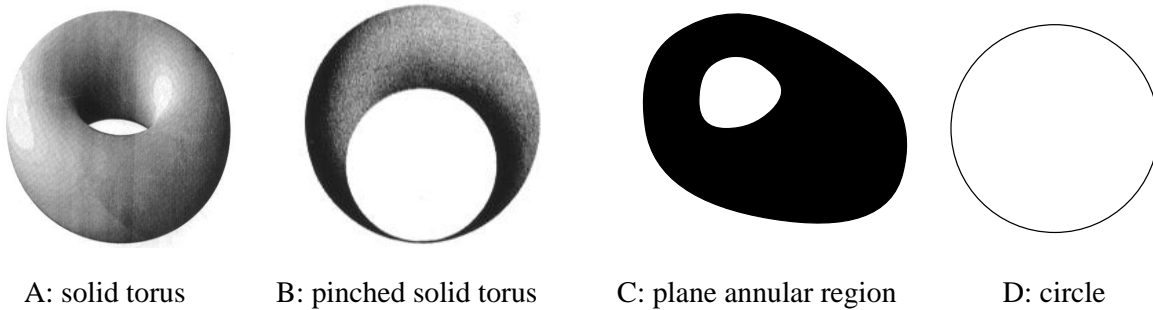


Fig. 4. Four objects which are all equivalent for Rel. 1, 3 and 4 but no two are homeomorphic because of dimension considerations.

3. A last important difference relies in orientation considerations [25]. Consider for instance Rel. 5 and Rel. 6. A homeomorphism of  $\mathbb{R}^3$  onto itself is either orientation preserving or orientation reversing. Consider now an isotopic deformation  $\{h_t\}$  of  $\mathbb{R}^3$ . The fact that the identity is orientation preserving combined with the continuity of  $H(t, P) = h_t(P)$  implies that  $h_t$  is orientation preserving  $\forall t \in [0, 1]$ . Hence Rel. 5 is only a necessary condition to Rel. 6. Practically, whereas an object and its mirror image under a reflection are not necessarily equivalent for Rel. 6, they are systematically equivalent for Rel. 5.

The exact link between Rel. 3 and Rel. 4 is not completely clear for us. Intuitively, Rel. 4 is more stringent because of orientation considerations similar to the ones described in point 3 above. Hence, another equivalent definition of Rel. 4 inspired from the definition of Rel. 3 could be construct by removing the possibility of homeo-

morphic link in the sequences of objects and complements. This idea will be exploited in the definition of equivalence between 3D binary images proposed further in the paper.

**Digital spaces** With regard to image processing requirements, the definition of topological equivalence relations between discrete objects comes up against the difficult transposition of notions like continuous deformations or homeomorphisms. A simple solution would consist in using continuous analogs but it seems rather difficult to infer in this way useful results for practical algorithms in 3D because of combinational complexity. Furthermore, such an approach raises the question of what algorithm to choose in order to get a continuous analog. An alternative to the use of continuous analogs is provided by the framework of cellular complexes advocated in [26], [27] as the only possible choice to manage image topology. This framework turns out to be a powerful

tool for constructing theoretical proofs for practical algorithms [28]. In our opinion, this framework would be appropriate for the transposition in the image world of the wealth of the notion of topological equivalence between continuous spaces described above. Indeed, an accurate management of local dimensions could allow the construction of a digital equivalent to isotopy type in continuous spaces which could be used for pattern recognition. This idea is related to the possibility of precisely defining chain points, simple surface points, volume points and all possible junctions between sets of different dimensions [29].

Intuitively, the level of topology preservation required by our segmentation problem relies in the usual rubber analogy: we want to deform without tearing or pasting a black and white piece of rubber including  $X$  (black) and  $X$  complement (white) until the black part shows  $Y$  and the white part shows  $Y$  complement. We do not need to include dimension considerations in this deformation process. Hence, the level of topological equivalence we need is related to homotopy type (to be more precise to Rel. 4 defined above), which can be managed with simpler and more usual treatments than those involved by cellular complexes.

In fact, a fruitful solution for defining the notion of homotopy in image analysis relies in results from algebraic topology. Algebraic topology stemmed from the will to use formal algebraic techniques to study topological spaces as it had been done for analytic geometry. To the spaces and continuous maps between them correspond respectively groups and group homomorphisms [25]. The analogy with analytic geometry, however, breaks down in one essential feature. Whereas the coordinate algebra of analytic geometry completely reflects the geometry, the algebra of topology is only a partial characterization of the topology. This means that a typical theorem of algebraic topology will read: if topological spaces  $X$  and  $Y$  are homeomorphic, then such algebraic condition is satisfied. The converse proposition, however, will generally be false. Thus, if the algebraic conditions are not satisfied, we know that  $X$  and  $Y$  are topologically distinct. If, on the other hand, they are fulfilled, we usually can conclude nothing. Nevertheless, whereas the bridge from topology to algebra is almost always a one-way

road, it results in a lot of useful results. Moreover, considering the relative simplicity of objects studied in image processing (objects with good local properties to be compared with complex objects like fractals), this one-way road could turn out to be a highway for this field.

One of the most important entities of algebraic topology is the fundamental group of a topological space  $X$ . This group is constructed from the notion of loop in  $X$  with base point  $P$ :

**DEF. 1 (CONTINUOUS LOOP IN  $X$ )** *A loop  $\gamma$  in  $X$  with base point  $P$  is a continuous mapping  $\gamma : [0, 1] \rightarrow X$  such that  $\gamma(0) = \gamma(1) = P$ .*

A trivial case is the constant mapping onto  $\{P\}$ .  $\gamma^{-1}$  denotes the loop obtained by traversing the loop  $\gamma$  backwards ( $\gamma^{-1}(x) = \gamma(1 - x)$ ) which is called the inverse of  $\gamma$ . The product  $\gamma_1 \cdot \gamma_2$  of two loops  $\gamma_1, \gamma_2$  with same base point  $P$  is defined by:  $\gamma_1 \cdot \gamma_2(x) = \gamma_1(2x)$  if  $x \in [0, \frac{1}{2}]$  and  $\gamma_1 \cdot \gamma_2(x) = \gamma_2(2x - 1)$  if  $x \in [\frac{1}{2}, 1]$ .

**REL. 7 (CONTINUOUS LOOPS HOMOTOPIC IN  $X$ )** *Two loops in  $X$   $\gamma_1, \gamma_2$  with the same base point  $P$  are homotopic in  $X$  if the mappings  $\gamma_1$  and  $\gamma_2$  are homotopic relatively to  $\{0, 1\}$  (see Def. A.6).*

Rel. 7 defines an equivalence relation compatible with the loop composition and the loop inverse defined above. The fundamental group of  $X$  with based point  $P$ , denoted by  $\Pi_1(X, P)$ , is the group formed by the equivalence classes of this relation among loops in  $X$  with base point  $P$  under the  $\cdot$  product operation. If  $P$  and  $Q$  belong to the same pathwise connected component of  $X$ ,  $\Pi_1(X, P)$  and  $\Pi_1(X, Q)$  are isomorphic (as a consequence, the base point  $P$  will be omitted in the following when we are only interested in properties of  $\Pi_1(X, P)$  as an abstract group). The importance of the fundamental group relies in the following result: if  $X$  and  $Y$  are pathwise connected spaces of the same homotopy type, then  $\Pi_1(X)$  and  $\Pi_1(Y)$  are isomorphic. A more informative result is the following [25]:

**THEOREM 1** *If  $X$  is pathwise connected and a subspace  $Y$  is a deformable retract of  $X$ , if  $i : Y \rightarrow X$  is the inclusion mapping, then  $\forall P \in Y$ ,  $i$  induces an isomorphism between  $\Pi_1(Y, P)$  and  $\Pi_1(X, P)$ .*

Theorem 1 is important for our purpose because, first the notion of loop is easily extended to binary images, and second the notion of continuous deformation (and hence homotopic mappings) can be more easily transposed for loops than for mappings defined on higher dimension spaces. Following the notation of [30] for conventional digital images, we assimilate now a 3D binary image  $I$  to  $(\mathbb{Z}^3, m, n, B)$  where  $B \subset \mathbb{Z}^3$  is the black point set (object),  $\mathbb{Z}^3 - B$  is the white point set (object complement), and  $(m, n) \in \{(6, 26), (26, 6)\}$  corresponds to the well-known dual connectivity choice allowing transposition of the classical Jordan theorem to the orthogonal lattice [31] (black points are said to be adjacent if they are  $m$ -connected and white points are said to be adjacent if they are  $n$ -connected). The complement of the 3D binary image  $I = (\mathbb{Z}^3, m, n, B)$  is  $\bar{I} = (\mathbb{Z}^3, n, m, \mathbb{Z}^3 - B)$ . A digital loop in  $B$  (resp.  $\mathbb{Z}^3 - B$ ) is simply a closed chain of adjacent black (resp. white) points. The notion of homotopic continuous loops (Rel. 7) has been transposed to the notion of equivalent digital loops in a discrete set  $X$  in different ways (see for instance the definition of digital deformation in [32]). Then, various non equivalent definitions of topology preserving transformations based on the preservation of such digital loop equivalence have been proposed [31], [32], [33]. These kind of topology preserving transformations are often called homotopic transformations in the field of mathematical morphology [31]. This transposition approach is formally extended to the definition of digital fundamental groups (DFG) of a digital image in [30]. A first definition of (DFG) relies on the standard notion of digital loop and on ad hoc local deformations of these loops aiming at transposing homotopic equivalence (Rel. 7). Kong proposes also a more general definition which applies to a wider range of digital picture kinds. For the simple kind of 3D digital images considered in this paper, this definition amounts to the following: Let  $I_B$  denote the union of black points of  $B$  and black adjacencies of  $I$ , namely the segments of  $\mathbb{R}^3$  corresponding to adjacencies between black points of  $B$  and let  $I_W$  denote the union of white points of  $\mathbb{Z}^3 - B$  and white adjacencies of  $I$ , namely the segments of  $\mathbb{R}^3$  corresponding to adjacencies between white points of  $\mathbb{Z}^3 - B$ .

**DEF. 2 (CONTINUOUS BLACK LOOPS)** *A continuous black loop of  $I$  with base point  $P \in B$  is a continuous mapping  $\gamma : [0, 1] \rightarrow I_B$  such that  $\gamma(0) = \gamma(1) = P$  and there exists  $k \in \mathbb{N}^*$  such that  $\forall i < k$ :*

1.  $\gamma(\frac{i}{k}) \in B$ ;
2.  $\gamma(\frac{i}{k})$  is equal or adjacent to  $\gamma(\frac{i+1}{k})$ ;
3.  $\gamma$  is linear on the closed interval  $[\frac{i}{k}, \frac{i+1}{k}]$ .

The link between continuous loops defined in 2 and the usual digital black loops is straightforward. Note that continuous black loops defined in Def. 2 are special cases of continuous loops in  $I_B$  or in  $\mathbb{R}^3 - I_W$  in the sense of Def. 4. Therefore, the following equivalence relation is defined:

**REL. 8 (CONTINUOUS LOOPS IN  $I_B$  EQUIVALENT IN  $I$ )** *Two continuous loops in  $I_B$  with base point  $P$  are said to be equivalent in  $I$  if they are homotopic in  $\mathbb{R}^3 - I_W$  in the sense of Rel. 7.*

Finally, note that the product of two continuous black loops of  $I$  is usually not a continuous black loop of  $I$  in the sense of Def. 2 but simply a continuous loop in  $I_B$  (nevertheless, another definition of continuous black loops composition copied from composition of digital loops could be used). This explains why the DFG of  $I$  with based point  $P \in B$ , denoted by  $\Pi(I, P)$ , is defined as the group formed by the equivalence classes of Rel. 8 among continuous loops in  $I_B$  with base point  $P$  under the  $\cdot$  product operation. This DFG definition allows Kong to propose a definition of thinning algorithms which preserve topology based on theorem 1. A simple extension of this definition which suppresses the localization constraint legitimately imposed to thinning, combined with ideas stemming from equivalence Rel. 3 and 4 definitions results in the definition of what we call homotopically equivalent 3D binary images.

**REL. 9 (HOMOTOPICALLY EQUIVALENT 3D BINARY IMAGES)** *Two images  $I_X = (\mathbb{Z}^3, m, n, X)$  and  $I_Y = (\mathbb{Z}^3, m, n, Y)$  ( $(m, n) \in \{(6, 26), (26, 6)\}$ ) are homotopically equivalent if there exists a sequence of images  $I_{B_0} = (\mathbb{Z}^3, m, n, B_0), I_{B_1} = (\mathbb{Z}^3, m, n, B_1), \dots, I_{B_k} = (\mathbb{Z}^3, m, n, B_k)$  such that  $B_0 = X, B_k = Y$ , and  $\forall i, 1 \leq i \leq k, B_i$  is obtained from  $B_{i-1}$  using one of the dual following ways:*

- a point set is added to  $B_{i-1}$  in such a way that:

1. each  $m$ -connected component of  $B_i$  contains exactly one  $m$ -connected component of  $B_{i-1}$ ;
  2. each  $n$ -connected component of  $\mathbb{Z}^3 - B_{i-1}$  contains exactly one  $n$ -connected component of  $\mathbb{Z}^3 - B_i$ ;
  3. for each point  $P \in B_{i-1}$ , the inclusion mapping  $i : B_{i-1} \rightarrow B_i$  induces a group isomorphism between  $\Pi(I_{B_{i-1}}, P)$  and  $\Pi(I_{B_i}, P)$ ;
  4. for each point  $P \in \mathbb{Z}^3 - B_i$ , the inclusion mapping  $i : \mathbb{Z}^3 - B_i \rightarrow \mathbb{Z}^3 - B_{i-1}$  induces a group isomorphism between  $\Pi(\overline{I_{B_i}}, P)$  and  $\Pi(\overline{I_{B_{i-1}}}, P)$ ;
- a point set is deleted from  $B_{i-1}$  in such a way that conditions dual to the previous ones are verified (duality with respect to white and black points).

It should be noted that Rel. 9 is only a definition which mimics as far as possible Rel. 3 (apart from homeomorphism link). An analogous definition applied to any continuous objects embedded in  $\mathbb{R}^3$  would a priori not systematically imply Rel. 3. Indeed nested connected components with inclusion inducing isomorphisms between fundamental groups is only a necessary condition to existence of a deformable retract between sets. Returning now to the work of Kong [30], it has been shown there that with the kind of images used in this paper, one can exhibit an algorithm to construct polyhedral continuous analogs  $C(I)$  with a set of very good properties with regard to topological analogy (especially isomorphism between  $\Pi(I, P)$  and  $\Pi_1(C(I), P)$  (resp.  $\Pi(\overline{I}, P)$  and  $\Pi_1(\mathbb{R}^3 - C(I), P)$ ) induced by inclusion between  $I_B$  and  $C(I)$  (resp. between  $I_W$  and  $\mathbb{R}^3 - C(I)$ ). Hence, an interesting problem is whether equivalence 9 between images implies Rel. 3 between these continuous analogs. This problem, which is far beyond the scope of this paper, should be related to the problem of determining whether a parallel thinning operator always preserves topology [34].

In the following, for the sake of simplicity, the term homotopy of a binary object  $\mathcal{O}$  will be employed to characterize the equivalence class of Rel. 9 to which belongs the 3D binary image which describes  $\mathcal{O}$ . Hence, 3D binary image transforma-

tions preserving object homotopy will be called homotopic deformations (the object being homotopically deformed).

For practical applications described in this paper, we use Rel. 9 in a very restricted way. Indeed, our homotopic deformations rely on the well-known concept of simple points, namely points that can change of color in a binary image without topology modifications. An homotopic deformation is then constructed as a sequence of simple point additions or deletions in the black point set, which is easy to carry out because efficient local characterizations of simple points exist [29], [35], [36], [37]. Whereas a number of different definitions of the notion of topology preservation in 3D binary images have been proposed in the literature, it turns out that exactly the same points are simple whichever definition is used [33] (differences occur only with parallel deformation algorithms changing color of several points at the same time). This surprising confusion with regard to topology preservation definition stems mainly from the considerable increase in complexity between 2D and 3D topology which has resulted in formalization difficulties (it should be noted that in 2D discrete homotopy is completely described by the tree of nested connected component of object and background (see Fig. 5) [31]; hence, in Rel. 9, conditions 1, 2 and duals are sufficient to define homotopy preserving deformations). The problem concerning continuous analogs raised previously could be addressed for simple points by constructing ad hoc deformation retracts for each configuration in the same spirit than in [23] for isotopy. Nevertheless, this work appears particularly cumbersome with regard to the number of configurations, all the more because the result seems intuitively true. Apart from homotopy preservation for continuous analogs, preservation of fundamental groups of continuous analogs defined in [33] could be a guideline to find a good justification for multiscale implementations of simple point based homotopic deformations. Difficulty lies in the behaviour of the algorithm of [33] producing continuous analogs relatively to multiscale point of view, but intuitively, for the simple kind of 3D binary images considered in this paper (images endowed with the (26, 6) dual connectivities), a simpler algorithm could be use, namely

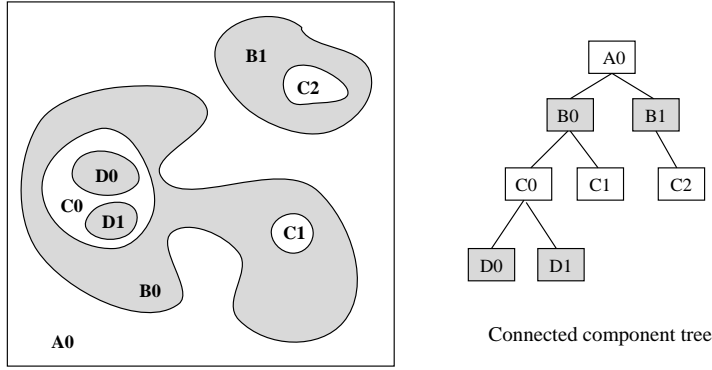


Fig. 5. Tree of the connected components of a finite object and of its complement in an infinite space: the tree root is the infinite connected component of the background; the remaining part of the tree is constructed with an alternance of object and background nested connected components.

for  $I = (\mathbb{Z}^3, 2\delta, 6, B)$ ,  $C(I) = \bigcup\{c(P) \mid P \in B\}$  where  $c(P)$  is a cube of side unity centered around  $P$ .

### 3.2. Homotopically deformable regions

We will now describe the main outlines of the homotopically deformable region (HDR) method before focusing on its application to the detection of the “gray matter/white matter interface”. An initial region endowed with a priori known topological properties is homotopically deformed according to Rel. 9 in order to minimize a global energy. This energy has the form of the Hamiltonian of a Gibbs random field (GRF) (the energy on which a Gibbs distribution relies), namely a clique potential sum. Like in deformable contour approaches, this energy is the sum of two terms: a regularization term which relies for instance on Ising model [38], and a data driven term which is a simple model of the noise process. Hence, analogy between HDR and deformable contour approaches is straightforward:

- The surface of the deformable region behaves like a deformable surface regularized by Ising model rather than by a differential term [19]. This results in a better detection of convoluted surfaces. Nevertheless, it should be noted that over-regularization problems still exist with regard to fine structures when using Ising model. Therefore specific applications could call for extension to 3D of adaptive Markovian regular-

ization models proposed in 2D (line processes [38], “chien” model [39])

- Data contribution to the global energy does not rely on potentials attracting the deformable surface towards edge points previously extracted by an edge detector but on intensity-based potentials acting on both delimited regions. In this way, one interface can be selected among several ones using differences between object intensities (or textures).

The analogy with deformable contour approaches can be extended by the introduction of a pression-like term corresponding to an external field in the GRF domain. The global energy is minimized using either a deterministic algorithm or a stochastic algorithm (e.g. simulated annealing). It should be noted that since topological constraints are included in the minimization process, the HDR method does not respect the “positivity constraint” of GRF and hence does not belong to the GRF class of methods (in a GRF framework, all the configurations corresponding to objects non homotopic to the initial object would have a null probability).

## 4. Segmentation

This section describes the different steps of an algorithm allowing segmentation of the union {CSF, gray matter} in a 3D MR image of the head (see Fig. 6) as an object homotopic to a solid ball with one cavity. This algorithm combines tools of 3D mathematical morphology with the HDR principle previously described.

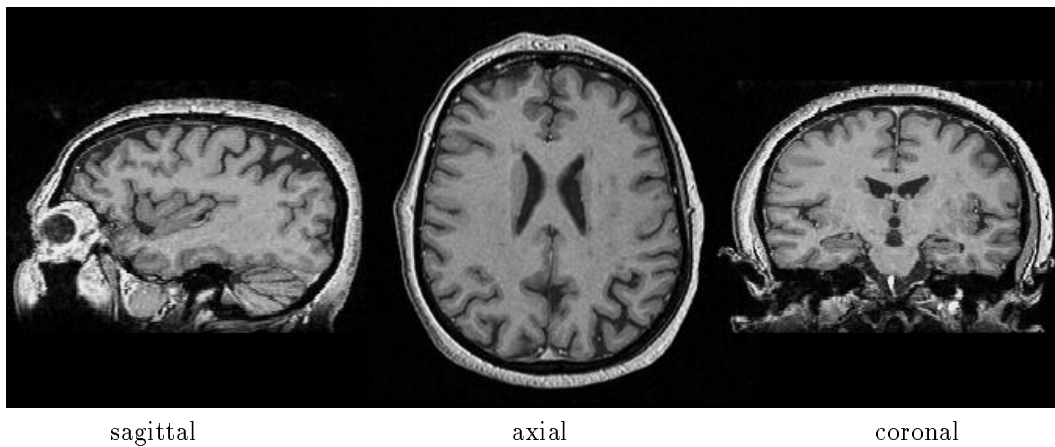


Fig. 6. Three orthogonal slices of the T1-weighted MR image (124 axial slices  $256 \times 256$ , pixel size: 1mm, slice thickness: 1.3mm, scanner: Signa GE 1.5 Tesla).

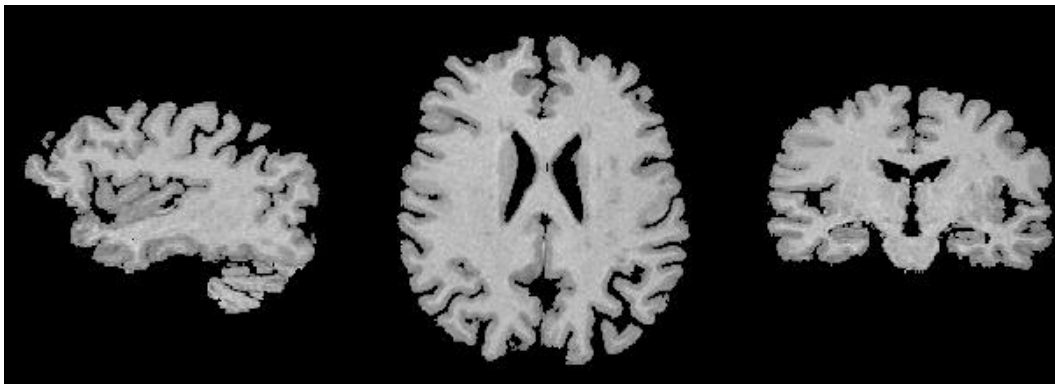


Fig. 7. Brain segmentation using 3D mathematical morphology (result of the reconstruction (cf. step 4.1.4)).

#### 4.1. Brain segmentation using 3D mathematical morphology

The first segmentation step produces, from the MR image (see Fig. 6), a binary object  $\mathcal{O}_{brain-CSF}$  whose surface corresponds to the brain hull. The structuring elements used to construct the morphological transformations [31] applied during this step are balls of anisotropic chamfer distances adapted to the voxel sizes of the MR image [40]. The following processes are applied sequentially.

##### 4.1.1 Binarization:

- A. a low threshold eliminates skull and CSF;
- B. a high threshold eliminates vascular system and fat.

These two thresholds are easily estimated from the image histogram.

**4.1.2 Erosion:** a 3D binary erosion (5mm) fully disconnects the brain from other tissues.

**4.1.3 Marker selection:** the largest 26-connected component is selected as a brain marker.

**4.1.4 Reconstruction:** a 3D dilation of the marker (same size as the erosion (cf. step 4.1.2)) conditionally to the result of the binarization (cf. step 4.1.1) reconstructs the brain (see Fig. 7).

**4.1.5 Closing:** a 3D closing (15mm) fills the sulci, the inter-hemispheric fissure and the ventricular system (an additional effect of this step is the recovering of narrow gyri truncated by previous steps).

**4.1.6 Cavity elimination:** the remaining cavities of  $\mathcal{O}_{brain-CSF}$ , detected as 6-connected components of the background not adjacent to the image border, are filled.

## Homotopic multiscale dilation

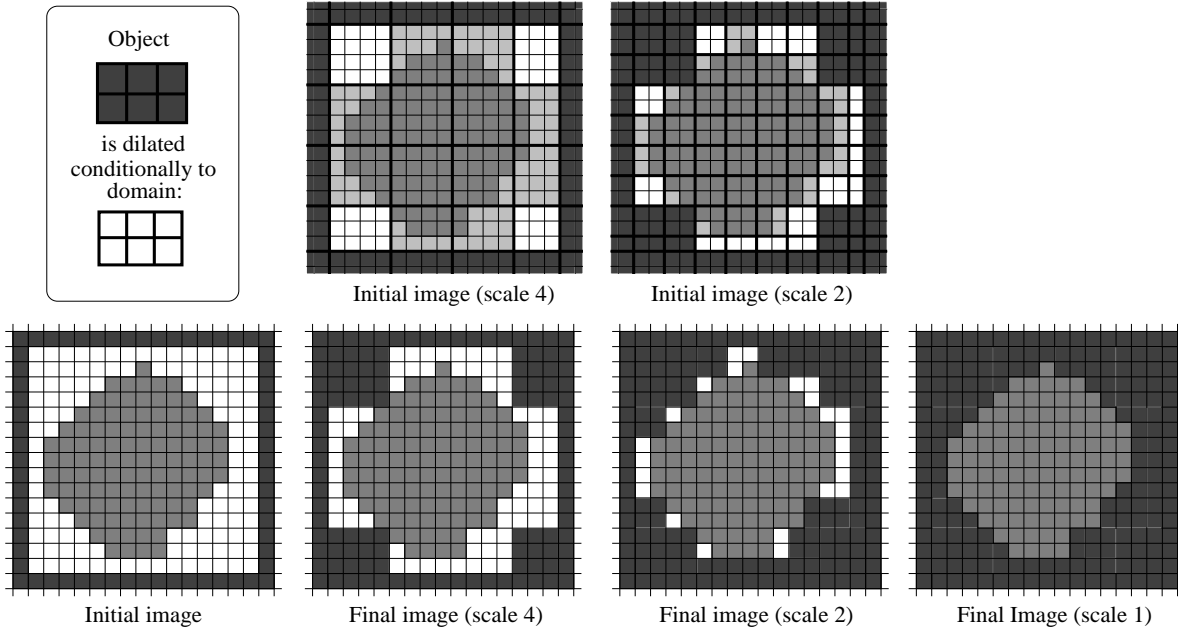


Fig. 8. 2D illustration (with  $(8, 4)$  dual connectivity pair) of the multi-scale implementation principle for homotopic dilation of the empty parallelepipedic box ( $\mathcal{O}_{hdr}^0$ ) bounding an object ( $\mathcal{O}_{brain-CSF}$ ) conditionally to object complement in the box interior ( $\mathcal{O}_{int}^0$ ). Note that since the box sizes are not necessarily of the form  $2^m$ , some of the voxels at scale  $n$  may not be cubic ( $n \times n \times n$ ). The homotopy preservation during scale transitions results intuitively from homotopy preservation for underlying continuous analogs (note that the only potential topological modifications would affect the  $\mathcal{O}_{hdr} / \mathcal{O}_{int}$  interface).

### 4.2. Segmentation of the union $\{\text{gray matter, CSF}\}$ using topology preserving deformations

The second segmentation step produces a binary object  $\mathcal{O}_{gray-CSF}$  which corresponds to the union of gray matter (cortex and some internal nuclei) and CSF. The object  $\mathcal{O}_{gray-CSF}$  is delimited by two interfaces: the brain hull (external) and the “gray matter/white matter” interface (internal). In order to increase the robustness of the following skeletonization step, both topological constraints and interface regularization are included in the segmentation process using the HDR method. The deformable region is initially endowed with the homotopy of a sphere (or a full ball with one cavity). This homotopy is preserved during all the deformation process. The segmentation is performed by a sequence of homotopic deformations. Each of these deformations is performed according to a front propagation, points

of a front being treated according to a classical raster scan. It should be noted that the result depends on this point visit order. In the following,  $\mathcal{O}_{hdr}$  denotes the homotopically deformable region,  $\mathcal{O}_{int}$  denotes the cavity of  $\mathcal{O}_{hdr}$  and  $\mathcal{O}_{ext}$  the outside.

**4.2.1 Initialization:** the initial deformable region  $\mathcal{O}_{hdr}^0$  is the empty parallelepipedic bounding box of  $\mathcal{O}_{brain-CSF}$  (cf. step 4.1), which has clearly the homotopy we want to impose.

**4.2.2 Detection of the brain hull:** the first homotopic deformation aims at detecting the brain hull. This cannot be done directly from  $\mathcal{O}_{brain-CSF}$  surface because of the potential presence of “tunnels” [23] in  $\mathcal{O}_{brain-CSF}$ .

**A. Homotopic multiscale conditional dilation:**  $\mathcal{O}_{hdr}^0$  is dilated until convergence conditionally to the complement of  $\mathcal{O}_{brain-CSF}$  in  $\mathcal{O}_{int}^0$ . Simple points are added to  $\mathcal{O}_{hdr}$  sequentially during a front propagation. The specific shape of  $\mathcal{O}_{int}^0$  with regard to the image lattice allows a multi-

## Homotopic multiscale erosion

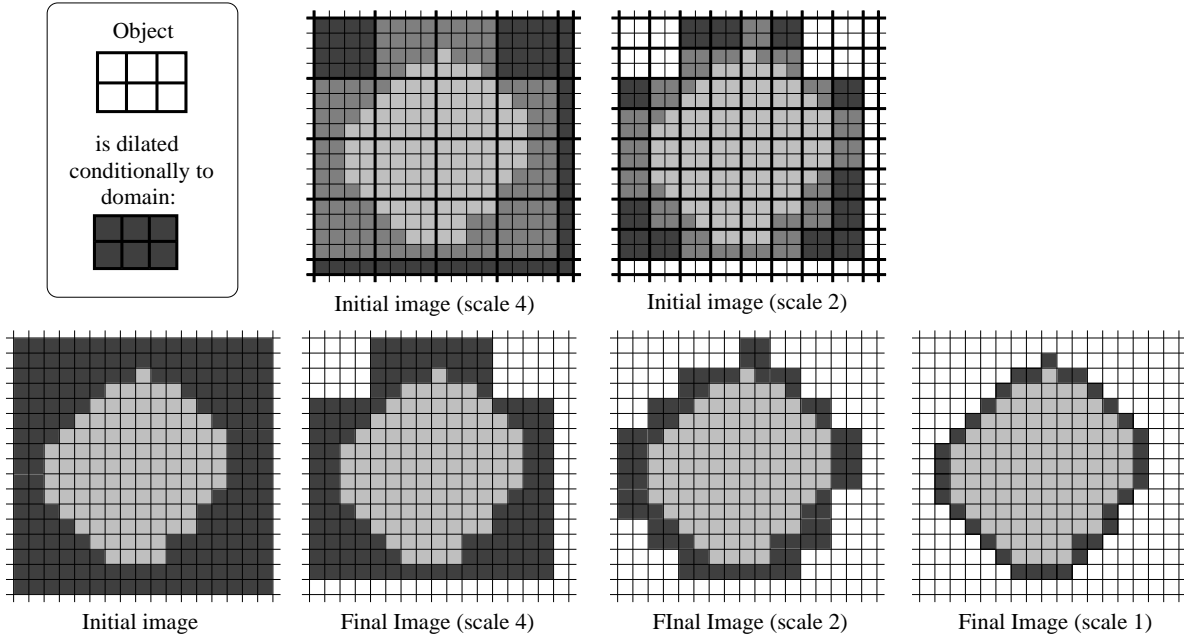


Fig. 9. 2D illustration (with  $(8, 4)$  dual connectivity pair) of the multi-scale implementation principle for homotopic erosion from outside ( $\mathcal{O}_{ext}^0$ ) of a hollow object ( $\mathcal{O}_{hdr}$ ) which external surface is parallelepipedic. This principle is slightly more complex than in Fig. 8 because the homotopic deformation is applied in fact to object  $\mathcal{O}_{ext}^0$ , but has nevertheless to preserve homotopy of object  $\mathcal{O}_{hdr}$  (the  $\mathcal{O}_{hdr} / \mathcal{O}_{int}$  interface has to be preserved). Note that since the parallelepiped sizes are not necessarily of the form  $2^m$ , some of the voxels at scale  $n$  may not be cubic ( $n \times n \times n$ ). The homotopy preservation during scale transitions results intuitively from homotopy preservation for underlying continuous analogs (note that the only potential topological modifications would affect the  $\mathcal{O}_{ext} / \mathcal{O}_{hdr}$  interface).

scale implementation of this homotopic dilation (see Fig. 8).

**B. Homotopic multiscale “conditional erosion”:**  $\mathcal{O}_{ext}^0$  is dilated until convergence conditionally to  $\mathcal{O}_{hdr}$ , any connection between  $\mathcal{O}_{ext}$  and  $\mathcal{O}_{int}$  being forbidden. Simple points are added to  $\mathcal{O}_{ext}$  sequentially during a front propagation. As for the transformation 4.2.2.A, the specific shape of  $\mathcal{O}_{ext}^0$  allows a multiscale implementation of this homotopic erosion (see Fig. 9). It should be noted that a simpler implementation could be obtained if the multi-scale process was applied simultaneously to dilation and erosion from the top to the bottom of the scale pyramid like in [41].

**4.2.3 Detection of the “gray matter/white matter” interface:** At the end of previous step,  $\mathcal{O}_{hdr}$  is constituted by a thin layer of points located at the level of the brain hull. Then  $\mathcal{O}_{hdr}$  is dilated conditionally to  $\mathcal{O}_{int}$ , according to the

HDR principle described in previous section, in order to reach the “gray matter/white matter” interface defined as the minimum of a global energy  $U$ . This energy is the sum of two components:

1. **A data driven component  $U_d$**  constituted by a sum of potentials attached to order one cliques. These potentials depend on statistical parameters estimated from the following steps:
  - A. The initial MR image is masked by  $\mathcal{O}_{brain-CSF}$  to get the gray level image *Masked*.
  - B. *Masked* is automatically classified in three classes (CSF, gray matter and white matter) using the K-means algorithm.
  - C. Means and standard deviations of the gray and white matter gray levels ( $m_G, \sigma_G, m_W$  and  $\sigma_W$ ) are estimated from the previous classification.

In the following,  $l(M)$  denotes the value of a point  $M$  in the binary image describing  $\mathcal{O}_{hdr}$  ( $l(M) = 1$  if  $M \in \mathcal{O}_{hdr}$ ,  $l(M) = 0$  otherwise),  $p(M)$  denotes the corresponding gray level value in *Masked* and  $C_M$  denotes the order one clique

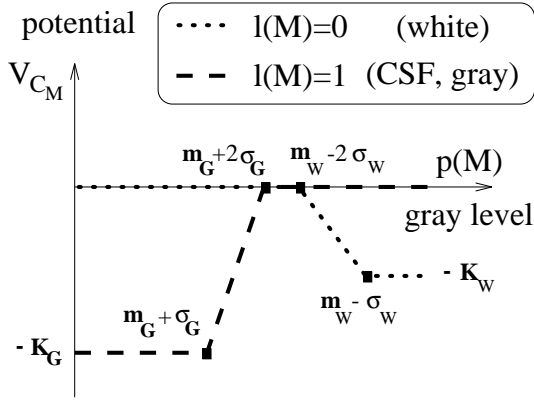


Fig. 10. **Data driven potentials:** it should be noted that this potential choice does not depend on the condition  $(m_G + 2\sigma_G) \leq (m_W - 2\sigma_W)$  which was nevertheless always verified in our experiments.

attached to  $M$ . The data driven potentials make up a very simple model of the likelihood that a gray level corresponds to a class (cf. Fig. 10):

$$U_d(l) = \sum_{C_M} V_{C_M}(l)$$

with:

$$\begin{aligned} \text{if } l(M) = 1, & \quad V_{C_M}(l) = -K_G f_G(p(M)), \\ \text{if } l(M) = 0, & \quad V_{C_M}(l) = -K_W f_W(p(M)), \end{aligned}$$

where  $K_G > 0$ ,  $K_W > 0$  and functions  $f_G$  and  $f_W$  are defined by:

$f_G$ :

$$\begin{aligned} x \in [0, m_G + \sigma_G], & \quad f_G(x) = 1; \\ x \in [m_G + \sigma_G, m_G + 2\sigma_G], & \quad f_G(x) = 1 - \frac{x - m_G - \sigma_G}{\sigma_G}; \\ x \in [m_G + 2\sigma_G, \infty], & \quad f_G(x) = 0; \end{aligned}$$

$f_W$ :

$$\begin{aligned} x \in [0, m_W - 2\sigma_W], & \quad f_W(x) = 0; \\ x \in [m_W - 2\sigma_W, m_W - \sigma_W], & \quad f_W(x) = 1 - \frac{m_W - \sigma_W - x}{\sigma_W}; \\ x \in [m_W - \sigma_W, \infty], & \quad f_W(x) = 1; \end{aligned}$$

**2. A regularization component  $U_r$**  constituted by Ising model [38] attached to order two cliques  $C_{M_1 M_2}$ , where  $M_1$  and  $M_2$  are 6-adjacent points of the binary image describing  $\mathcal{O}_{hdr}$ :

$$U_r(l) = \sum_{C_{M_1 M_2}} V_{C_{M_1 M_2}}(l),$$

with  $V_{C_{M_1 M_2}}(l) = -K_I \delta_{l(M_1)l(M_2)}$ ,  $K_I > 0$ ,

where  $\delta_{xy}$  denotes the Kronecker symbol.

The weighting constants  $K_G$ ,  $K_W$  and  $K_I$  are chosen from simple considerations about the local structure of the “ $\mathcal{O}_{hdr}/\mathcal{O}_{int}$ ” interface. The addition of a simple point  $M$  to  $\mathcal{O}_{hdr}$  gives the following energy variation:

$$\begin{aligned} \Delta U &= \Delta U_r + \Delta U_d \\ &= -K_I(n_v^1 - n_v^0) \\ &\quad + K_W f_W(p(M)) - K_G f_G(p(M)), \end{aligned} \quad (1)$$

where  $n_v^i$  is the number of 6-neighbours  $P$  of  $M$  which verify  $l(P) = i$  ( $i \in \{0, 1\}$ ).

**$K_G$ :** In order to prevent the regularization component from hampering the dilation of the deformable region, we impose  $\Delta U < 0$  when  $p(M) < m_G + \sigma_G$ . In consequence, if we assume  $p(M) < m_W - 2\sigma_W$ , we get from eq. 1:

$$\Delta U = -K_I(n_v^1 - n_v^0) - K_G \leq 4K_I - K_G,$$

because we have necessarily  $n_v^1 \geq 1$ . Therefore we choose:

$$K_G = 4K_I + \epsilon \text{ with } \epsilon \ll K_I. \quad (2)$$

**$K_W$ :** In order to control the regularization effect on the deformable region interface, we impose  $\Delta U < 0$  when  $n_v^1 \geq 4$ . In such a configuration, we get from eq. 1:

$$\Delta U \leq -2K_I + K_W.$$

Therefore, we choose:

$$K_W = 2K_I - \epsilon \text{ with } \epsilon \ll K_I. \quad (3)$$

Once relations 2 and 3 are imposed,  $K_I$  can be chosen arbitrarily.

The minimization of  $U$  is performed using a deterministic algorithm similar to the iterated conditional modes [42]: during a front propagation, simple points are added to  $\mathcal{O}_{hdr}$  sequentially, an addition occurring each time it produces an energy decrease. It should be noted that this algorithm only gives a local minimum of  $U$ , which has turned out to be sufficient, nevertheless, to obtain very good segmentation results (see Fig. 11). Until now, the method has been successfully tested with fifteen different MR images and various acquisition parameters but slice thickness systematically



Fig. 11. Segmentation of the union {gray matter, CSF} using the homotopically deformable region method. An effect of the topological constraint included in the segmentation process can be observed at the level of the ventricular system: this constraint prevents several excrescences (related to ventricular system anatomy) of the deformable region from connecting themselves (which is not a problem since we are only interested in the sulci).

lower than 1.5 mm. This set of experiments have shown especially robust behaviour even with some particularly noisy images. A slight difficulty has been observed in a few cases at the level of inter-hemispheric fissure which was due to failure of the initial morphological processings (see Sect. 4.1) with respect to elimination of sinus. This difficulty resulted in a few deformations of the skeleton computed by the following steps. Some additional experiments have been performed with images yielded by older scanners producing a larger slice thickness (3mm). These experiments have shown that with slight adaptations (interpolation towards a more isotropic lattice), acceptable results can be obtained for the whole cortex apart from regions where folds are parallel to the slice plane. In such regions, some folds can be mixed because of partial volume effect.

## 5. Construction of the attributed relational graph

This section describes the construction of the ARG representing the cortex topography from the 3D skeleton of the binary object  $\mathcal{O}_{gray-CSF}$ .

### 5.1. Homotopic skeletonization

The 3D skeleton of  $\mathcal{O}_{gray-CSF}$  is obtained using a homotopic thinning which does not preserve 3D curves, thus allowing a first level of pruning. This

algorithm relies on the topological classification recently proposed by Malandain et al. [29]. The classification of an object point  $M$  depends only on two numbers:

$$C^* = NC_{ad}^{26}[\mathcal{O} \cap N_{26}^*(M), M]$$

$$\bar{C} = NC_{ad}^6[\bar{\mathcal{O}} \cap N_{18}^*(M), M]$$

where  $\mathcal{O}$  is the object,  $\bar{\mathcal{O}}$  is the object complement,  $N_c^*(M)$  is the neighbourhood of  $M$  for the  $c$ -connectivity ( $M$  excluded), and  $NC_{ad}^c[A, M]$  is the number of  $c$ -connected components of  $A$  adjacent to  $M$  for the  $c$ -connectivity. The different topological classes for 3D points are (see Fig. 12):

- A. interior: .....  $\bar{C} = 0$  ;
- B. isolated: .....  $C^* = 0$  ;
- C. border: .....  $\bar{C} = 1, C^* = 1$  ;
- D. curve: .....  $\bar{C} = 1, C^* = 2$  ;
- E. curves: .....  $\bar{C} = 1, C^* > 2$  ;
- F. surface: .....  $\bar{C} = 2, C^* = 1$  ;
- G. surface-curve: ....  $\bar{C} = 2, C^* \geq 2$  ;
- H. surfaces: .....  $\bar{C} > 2, C^* = 1$  ;
- I. surfaces-curve: .....  $\bar{C} > 2, C^* \geq 1$ .

A rapid sketch of this homotopic thinning is the following:

1. Initial topological classification of the points of  $\mathcal{O}_{gray-CSF}$ ; the points of types {F,G,H,I} will be undeletable during all the following steps;
2. Then, the following algorithm is iterated until convergence:

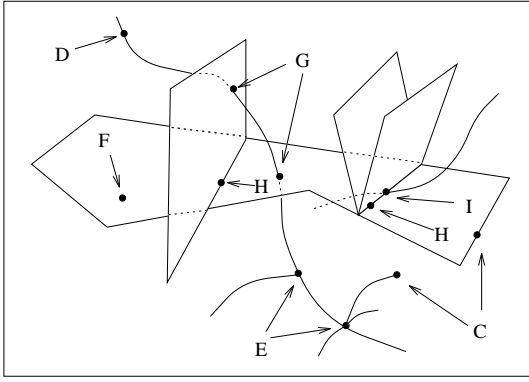


Fig. 12. Exhaustive topological classification of points for a 3D object considered in 26-connectivity [29]. Border points are equivalent to simple points [35].

for  $d$  being successively one of the 6 directions of the 6-connectivity [43], [44]:

- (a) Detection of the deletable points whose  $d^{th}$  6-neighbour is in the background;
  - (b) Sequential deletion of the deletable points when they are simple points;
  - (c) New topological classification of the remaining deletable points; the points of types  $\{F, G, H, I\}$  become undeletable.
3. A second level of homotopic pruning dedicated to remaining 3D curves is performed: simple points of the object with only one 26-neighbour are iteratively deleted. A third level of homotopic pruning dedicated to little surface parts will occur during the following skeleton segmentation step. An instance of final skeleton is proposed in Fig. 14.

## 5.2. Segmentation in simple surfaces

The 3D skeleton of  $\mathcal{O}_{gray-CSF}$  is segmented in simple surfaces, external brain surface and inter-hemispheric fissure. These skeleton subsets correspond to ARG nodes. Intuitively, a simple surface is a point set which separates locally the background in two connected components. Since the junction classes (types G, H, I (cf. Fig. 12)) of the topological classification do not correspond to the exhaustive set of junction points, simple surfaces cannot be considered as connected components of surface points (type F). Therefore, they are defined as the classes of the following equiva-

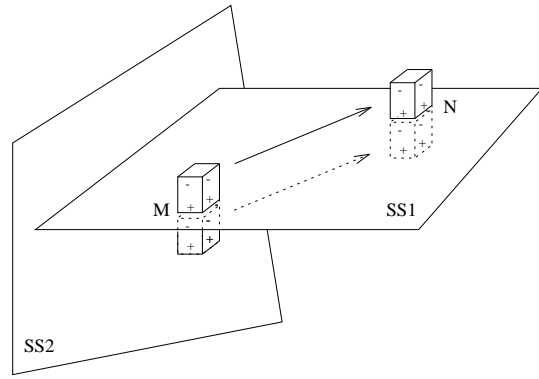


Fig. 13. The simple surfaces are defined as the classes of an equivalence relation between surface points (type F of Fig. 12) [29]. Intuitively, two surface points  $M$  and  $N$  are in relation if and only if two magnets located on both side of the surface can be moved from  $M$  to  $N$  without coming unstuck.

lence relation between surface points (type F) (see Fig 13) [29]: with the notations of Fig. 12, for a point  $M \in \mathcal{O}$  of type F,  $B_M$  and  $C_M$  denote the two 6-connected components of  $\overline{\mathcal{O}} \cap N_{18}^*(M)$  6-adjacent to  $M$ . Two points  $M$  and  $N$  of type F are in relation if and only if there exists a 26-path  $M_0, M_1, \dots, M_n$  of points of type F, with  $M_0 = M$ ,  $M_n = N$ , such that  $\forall i, 0 \leq i < n$ , one of the two following conditions is verified:

$$B_{M_i} \cap B_{M_{i+1}} \neq \emptyset \text{ and } C_{M_i} \cap C_{M_{i+1}} \neq \emptyset ;$$

or

$$B_{M_i} \cap C_{M_{i+1}} \neq \emptyset \text{ and } C_{M_i} \cap B_{M_{i+1}} \neq \emptyset .$$

The segmentation process itself consists of the following steps, which produce the ARG nodes and “topological relations”:

1. Detection of the brain external surface  $\mathcal{S}_{brain}$  as the set of skeleton points 6-adjacent to  $\mathcal{O}_{ext}$ . In the following,  $\mathcal{S}_{ulci}$  denotes the remaining part of the skeleton.
2. Segmentation of  $\mathcal{S}_{ulci}$  surface points in simple surfaces ( $SS$ s) (see Fig. 14 and 15).
3. Detection of  $SS$  internal borders (border points of the skeleton (type C) 26-adjacent to the  $SS$  surface points) which correspond mainly to fold bottom.
4. Homotopic pruning of little  $SS$ s (when a  $SS$  is constituted by less than 5 surface points, its surface and border points are sequentially deleted if they are simple points).

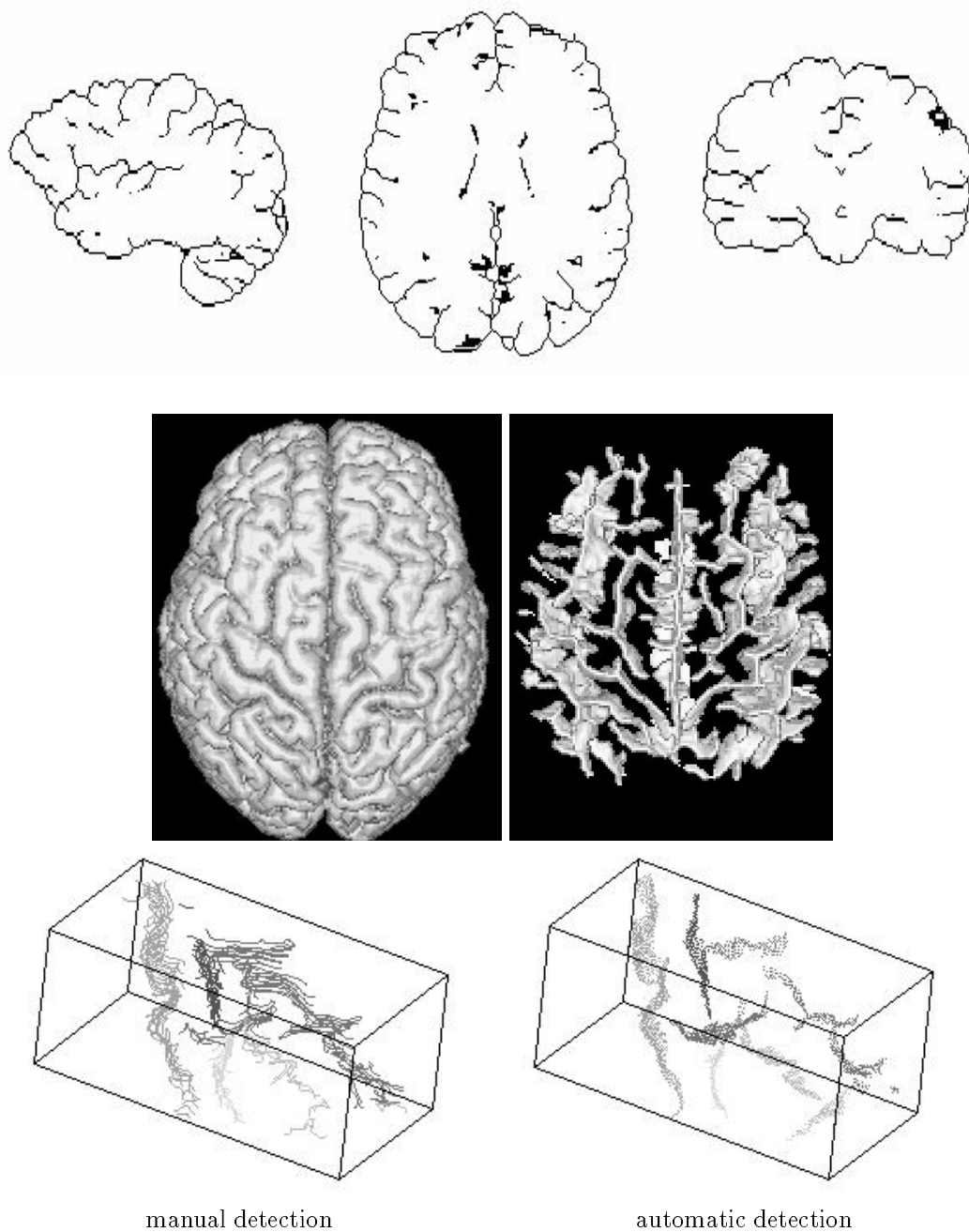


Fig. 14. *top*: Three orthogonal slices of the 3D skeleton of  $\mathcal{O}_{gray-CSF}$  (see Fig 11). Note the difficulty to catch topology from slices. *middle*: 3D rendering of the brain surface and of a part of the corresponding skeleton. *bottom*: 3D comparison of the automatic and manual detection of a cortical fold set (same folds as in Fig. 15).

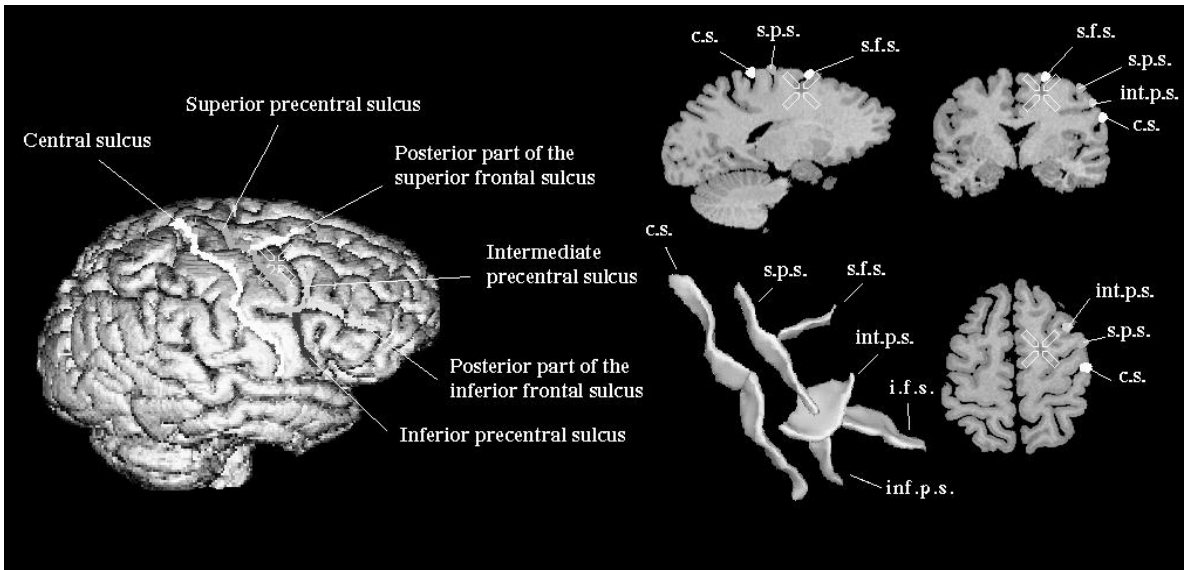


Fig. 15. Superimposition of junctions between simple surfaces and brain external surface in a 3D rendering of the brain and in 3 orthogonal slices [5]. A 3D rendering of the corresponding simple surface set is also proposed [6].

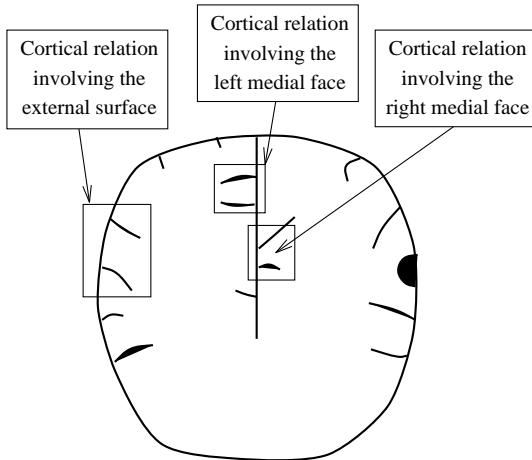


Fig. 16. Three types of cortical relations are inferred from three generalized Voronoï diagrams, according to the cortical part involved in the relation.

5. Detection of junctions between  $SS$ s and between a  $SS$  and  $\mathcal{S}_{brain}$  (a junction is a set of skeleton points 26-adjacent to two surfaces of interest; junctions of higher order are not considered). A pair of surfaces connected by a junction corresponds to an ARG topological relation ( $\rho_T$ ) (see Fig. 15).
6. Detection of the inter-hemispheric fissure  $\mathcal{P}_{med}$ : a subset of  $SS$ s is selected according to a priori knowledge about the brain orientation;  $\mathcal{P}_{med}$  is then detected as a connected component of the

graph induced by the junctions  $\rho_T$ 's in this  $SS$  subset. This process is unfortunately not fully satisfactory yet because in some cases, a few  $SS$ s of  $\mathcal{P}_{med}$  include a sulcus part (this results from deficiency of the topological segmentation principle when too many simple surfaces intersect in the same skeleton region). We will have to split such  $SS$ s according to curvature properties.  $SS$ s and internal junctions of  $\mathcal{P}_{med}$  are merged in a single surface, junctions with other  $SS$ s and  $\mathcal{S}_{brain}$  being rearranged in accordance.

### 5.3. ARG "Cortical relations"

In addition to topological relations, the ARG includes "cortical relations"  $\rho_C$ 's which can be considered as neighbourhood relationships. Intuitively, these relations correspond mainly to  $SS$  pairs forming a gyrus and  $SS$  pairs belonging to the same interrupted sulcus. Three kinds of cortical relations can occur, according to the part of the cortex involved in the relation: the external cortex or the right and left medial cortex (see Fig. 16). These relations are inferred from adjacencies of three generalized Voronoï diagrams. For instance, the relations involving the external

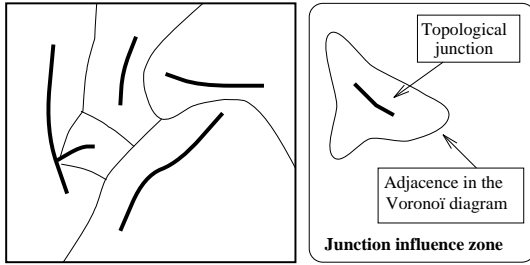


Fig. 17. A glimpse of a generalized Voronoi diagram computed conditionnally to a skeleton subset ( $\mathcal{S}_{brain}$  or  $\mathcal{P}_{med}$ ), for the junctions between the  $SS$ s and this subset (the figure represents a plane projection of a diagram part). The distance used to compute the diagram is a geodesic chamfer distance. Cortical relations are equivalent to adjacences in such a diagram.

surface are inferred from the diagram computed conditionnally to  $\mathcal{S}_{brain}$  for the junctions  $\rho_T$ 's between  $\mathcal{S}_{brain}$  and  $SS$ s (see Fig. 17).

#### 5.4. Construction of the attributed relational graph

An ARG  $\mathcal{G}$  is then constructed in order to represent synthetically the results of the previous segmentation steps. A subgraph of such an ARG corresponding to a sulcus is described in Fig. 18. Formally, an ARG is represented by the 6-tuple  $\mathcal{G} = (\mathcal{N}, \mathcal{R}, \sigma_{\mathcal{N}}, \sigma_{\mathcal{R}}, \lambda_{\mathcal{N}}, \lambda_{\mathcal{R}})$ , where:

$\mathcal{N}$  is the node set;

$\mathcal{R}$  is the relation set;

$\sigma_{\mathcal{N}} : \mathcal{N} \rightarrow \mathcal{S}_{\mathcal{N}} = \{SS, \mathcal{S}_{brain}, \mathcal{P}_{med}\}$  is a function called node syntactic interpreter;

$\sigma_{\mathcal{R}} : \mathcal{R} \rightarrow \mathcal{S}_{\mathcal{R}} = \{\rho_T, \rho_C\}$  is a function called relation syntactic interpreter;

$\lambda_{\mathcal{N}} : \mathcal{N} \rightarrow E(At_{\mathcal{N}})$  is a function called node semantic interpreter;

$\lambda_{\mathcal{R}} : \mathcal{R} \rightarrow E(At_{\mathcal{R}})$  is a function called relation semantic interpreter.

$At_{\mathcal{N}}$  is a set of semantic attributes describing nodes;

$At_{\mathcal{R}}$  is a set of semantic attributes describing relations;

$E(At_x)$  is the set of all semantic descriptions using semantic attributes of  $At_x$ .

A semantic description of  $E(At_x)$  is a set of pairs (attribute, attribute value), each attribute of  $At_x$  appearing at most in one pair. A semantic attribute reserved to instances of only one syntactic type  $t$  will be noted  $t$ -name. These seman-

tic attributes have been chosen in order to endow the ARG nodes and relations with a pertinent synthetic description sufficient to allow the sulcus identification. These various attributes are:

$At_{\mathcal{N}} = \{SS\text{-size}, SS\text{-center}, SS\text{-orientation}, SS\text{-depth}\};$

$At_{\mathcal{R}} = \{\rho_T\text{-length}, \rho_T\text{-direction}, \rho_C\text{-size}\};$

where:

- $SS$ -size corresponds to the number of points in a  $SS$ ;
- $SS$ -center corresponds to the center of gravity of a  $SS$ ;
- $SS$ -orientation corresponds to the normal of the plan which approximates a  $SS$  in a mean square sense;
- $SS$ -depth corresponds to the maximal distance geodesic to the skeleton from a  $SS$  point to  $\mathcal{S}_{brain}$  (computed from an anisotropic geodesic chamfer distance);
- $\rho_T$ -length corresponds to the number of points of a thinned topological junction;
- $\rho_T$ -direction corresponds to the direction of the straight line which approximates a topological junction in a mean square sense;
- $\rho_C$ -size corresponds to the size of an influence zone in a second level of generalized Voronoi diagram. One such diagram is computed for each of the three kinds of  $\rho_C$ s (see Fig. 16). For instance, for  $\mathcal{S}_{brain}$  based cortical relations, the diagram is computed conditionally to the complement in  $\mathcal{S}_{brain}$  of the union of the junctions  $\rho_T$ 's between  $\mathcal{S}_{brain}$  and  $SS$ s, for the different subsets of the skeleton by influence zone (SKIZ) dual of the first Voronoi diagram (see Fig. 17) which represent cortical relations (the smallest cortical relations according to the associated SKIZ subset size are not taken into account during this computation). This attribute aims at representing gyrus size.

## 6. CONCLUSION

We have presented in this paper a robust algorithm allowing the construction of an attributed relational graph representing the cortical topography from a 3D MR image. The key feature of this algorithm is the homotopically deformable region principle which can be viewed as a dual alternative to the widely used deformable contour

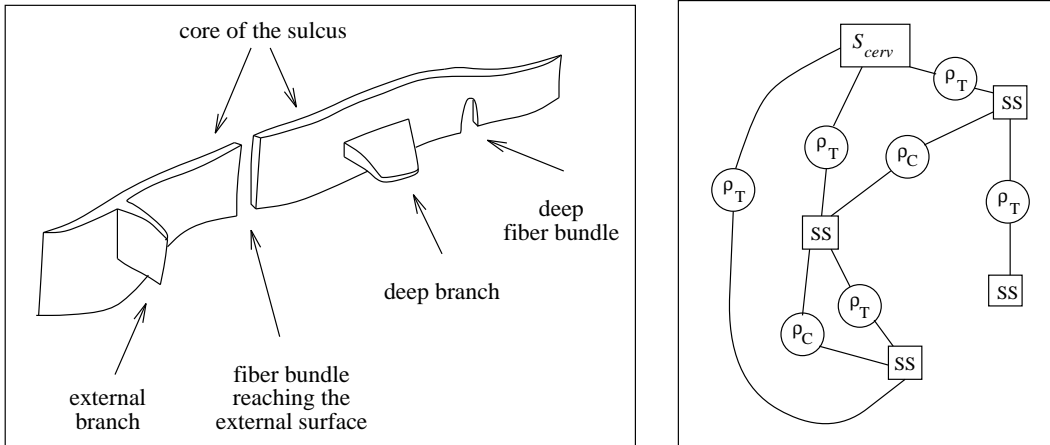


Fig. 18. A sulcus of the external face of an hemisphere and its representation in the ARG. This sulcus is interrupted by a fiber bundle allowing communication between the two delimited gyri.

paradigm. This framework turns out to be better adapted to detection of convoluted interfaces and allows introduction of topological knowledge in region based segmentation methods. The HDR method has been recently extended to images including more than two regions [41]. It has been shown that by using the topological arrangement of objects, the HDR principle can discriminate objects of similar intensities. An application consisting in head tissue classification in 3D MR images has been described. This experiment has shown that the HDR framework is especially powerful for segmentation applications which require management of several deformable objects according to various kind of a priori knowledge.

In order to perform anatomical studies on the inter-individual variability of the cortical topography, various 3D visualization tools allowing navigation in the relational graphs described in this paper have been developed [5], [6]. Hence, original explanations of this variability have been proposed and a consistent sulcus identification methodology has been designed [7], [8]. We are working today on the constitution of a large database of graphs in which the cortical sulci are identified using this methodology. A generic structural model of the cortical topography including various statistical estimations of the inter-individual variability is inferred from the database [9], [10]. This model is the core from which our present works on the automatic recognition of the cortical sulci are developed [9], [10]. This automatic recogni-

tion is achieved today for the main sulci with a database of only eight brains. Anatomical studies performed during our database constitution have shown that the cortical representation described in this paper was insufficient to address properly recognition of more variable sulci. Indeed, the addition in ARGs of a third kind of relation representing deep white matter fiber bundles is required (see Fig. 18). Therefore, we intend to perform detection of these fiber bundles as relevant local minima of the sulcus depth along the sulcus bottom. Then we will try to discover to which extent the sulcus recognition is well-founded. Indeed, we do not know today if the identification of any cortical fold is possible.

## Appendix A

### Standard definitions

In this appendix are recalled a few standard definitions on which rely the different topological equivalence relations between continuous objects embedded in  $\mathbb{R}^3$  proposed in section 3.1.

DEF. A. 1 (HOMEOMORPHISM) A *homeomorphism* between two topological spaces  $X$  and  $Y$  is a continuous mapping  $f : X \rightarrow Y$  with continuous  $f^{-1}$ .

DEF. A. 2 (DEFORMATION) A *deformation* of a topological space  $X$  is a family of mappings  $h_t : X \rightarrow X$ ,  $0 \leq t \leq 1$  such that  $h_0$  is the identity

and the function  $H$  defined by  $\forall t \in [0, 1] \forall P \in X$ ,  $H(t, P) = h_t(P)$  is simultaneously continuous in  $t$  and  $P$ .

DEF. A. 3 (ISOTOPIC DEFORMATION) A deformation of  $X$  is isotopic if  $\forall t \in [0, 1]$ ,  $h_t$  is a homeomorphism.

DEF. A. 4 (ISOTOPY TYPE) Two objects  $X$  and  $Y$  of  $\mathbb{R}^3$  are said to belong to the same isotopy type if there exists an isotopic deformation  $\{h_t\}$  of  $\mathbb{R}^3$  such that  $h_1 X = Y$ .

DEF. A. 5 (HOMOTOPIC MAPPINGS, HOMOTOPY) Let  $f_0$  and  $f_1$  be two continuous mappings from space  $X$  to space  $Y$ .  $f_0$  is homotopic to  $f_1$  if there exists a family of mappings  $h_t : X \rightarrow Y$ ,  $0 \leq t \leq 1$  such that  $h_0 = f_0$ ,  $h_1 = f_1$  and the function  $H$  defined by  $\forall t \in [0, 1] \forall P \in X$ ,  $H(t, P) = h_t(P)$  is simultaneously continuous in  $t$  and  $P$ .  $H$  is a homotopy from  $f_0$  to  $f_1$ .

DEF. A. 6 (HOMOTOPIC MAPPINGS RELATIVELY TO A SUBSPACE) Let  $f_0$  and  $f_1$  be two continuous mappings from space  $X$  to space  $Y$  and let  $A$  be a subspace of  $X$ .  $f_0$  is homotopic to  $f_1$  relatively to  $A$  if there exists a homotopy  $H$  from  $f_0$  to  $f_1$  such that  $\forall t \in [0, 1] \forall P \in A$ ,  $H(t, P) = f_0(P) = f_1(P)$ .

DEF. A. 7 (RETRACTION, RETRACT) A subspace  $Y$  of  $X$  is a retract of  $X$  if there exists a continuous mapping  $r : X \rightarrow Y$  such that  $\forall P \in Y$ ,  $r(P) = P$ .  $r$  is a retraction of  $X$  onto  $Y$ .

DEF. A. 8 (DEFORMABLE RETRACT) A subspace  $Y$  of a topological space  $X$  is a deformable retract of  $X$  if there exists a retraction of  $X$  onto  $Y$  homotopic to identity in  $X$  relatively to  $Y$ .

DEF. A. 9 (HOMOTOPY TYPE) Two objects  $X$  and  $Y$  of  $\mathbb{R}^3$  are of the same homotopy type if there exists a finite sequence  $X = X_0, X_1, \dots, X_n = Y$  of objects such that for each  $i = 1, \dots, n$ , either  $X_{i-1}$  and  $X_i$  are homeomorphic, or  $X_i$  is a deformation retract of  $X_{i-1}$ , or vice-versa (an equivalent more usual definition is based on the existence of continuous mappings  $f : X \rightarrow Y$  and  $g : Y \rightarrow X$  such that  $g \circ f$  and  $f \circ g$  are respectively homotopic to identity of  $X$  and  $Y$  (see [45] for proof).)

## References

1. J.-F. Mangin, V. Frouin, I. Bloch, B. Bendriem, and J. Lopez-Krahe. "Fast nonsupervised 3D registration of PET and MR images of the brain," *J. Cereb. Blood Flow Metab.*, vol. 14(5), pp. 749–762, 1994.
2. J. Talairach and P. Tournoux. *Co-Planar Stereotaxic Atlas of the Human Brain. 3-Dimensional Proportional System: An Approach to Cerebral Imaging*. Thieme Medical Publisher, Inc., Georg Thieme Verlag: Stuttgart, New York, 1988.
3. M. Ono, S. Kubik, and C. D. Abernethy. *Atlas of the Cerebral Sulci*. Georg Thieme Verlag, 1990.
4. A. Evans. "3D multimodality human brain mapping: past, present and future," in *Quantification of Brain Function. Tracer Kinetics and Image Analysis in Brain PET*, Elsevier Science, 1993, pp. 373–389.
5. V. Frouin, J.-F. Mangin, J. Régis, and B. Bendriem. "A 3D editor of the cortical sulcal topography," in *VIIth. IEEE Symp. on Computer-Based Medical Systems*, Winston Salem, USA, 1994, pp. 323–328.
6. J.-F. Mangin, V. Frouin, I. Bloch, J. Régis, Y. Samson, and J. Lopez-Krahe. "3-D visualization of the cortical sulcal topography," in *VIIIth. Conf. on Computer Assisted Radiology*, Winston Salem, USA, 1994, pp. 179–184.
7. J. Régis. *Anatomie sulcale profonde et cartographie fonctionnelle du cortex cérébral*. MD Thesis, Université d'Aix-Marseille II, France, 1994.
8. J. Régis, J.-F. Mangin, V. Frouin, F. Sastre, L. C. Peragut, and Y. Samson. "Cerebral cortex generic model for cortical localization and preoperative multimodal integration in epilepsy surgery," *Stereotactic and Functional Neurosurgery*, in press.
9. J.-F. Mangin, J. Régis, I. Bloch, V. Frouin, Y. Samson, and J. Lopez-Krahe. "A Markovian random field based random graph modelling the human cortical topography," in *First Int. Conf. on Computer Vision, Virtual Reality and Robotics in Medicine*, vol. 905 of *Lecture Notes in Computer Science*, Springer-Verlag Nice, France, 1995, pp. 177–183.
10. J.-F. Mangin. *Mise en correspondance d'images médicales 3D multi-modalités multi-individus pour la corrélation anatomo-fonctionnelle cérébrale*. PhD Thesis, École Nationale Supérieure des Télécommunications, Paris, France, 1995.
11. M. Joliot. *Traitement du signal de résonance magnétique nucléaire in vivo*. PhD thesis, Université de Paris-Sud, Orsay, France, 1992.
12. M. Desvignes, H. Fawal, M. Revenu, D. Bloyet, J. M. Travère, P. Allain, and J. C. Baron. "Calcul de la profondeur en un point des sillons du cortex sur des images RMN tridimensionnelles," in *Quatorzième Colloque GRETSI*, Juan-les-Pins, France, 1993, pp. 1267–1270.
13. J. P. Thirion and A. Gourdon. "Computing the differential characteristics of iso-density surfaces," *Computer Vision and Image Understanding*, vol. 61(2), pp. 190–202, 1995.

14. G. Székely, Ch. Brechbühler, O. Kübler, R. Ogiewicz, and T. Budinger. "Mapping the human cerebral cortex using 3D medial manifolds," in *SPIE Visualization in Biomedical Computing*, vol. 1808, 1992, pp. 130–144.
15. J. C. Bezdec, L. O. Hall, and L. P. Clarke. "Review of MR image segmentation techniques using pattern recognition," *Medical Physics*, vol. 20(4), pp. 1033–1048, 1993.
16. C. Li, D. B. Goldgof, and L. O. Hall. "Knowledge-based classification and tissue labeling of MR images of human brain," *IEEE Trans. on Medical Imaging*, vol. 12(4), pp. 740–750, 1993.
17. T. Taxt and A. Lundervold. "Multispectral analysis of the brain using magnetic resonance imaging," *IEEE Trans. on Medical Imaging*, vol. 13(3), pp. 470–481, 1994.
18. Z. Liang, J. R. MacFall, and D. P. Harrington. "Parameter estimation and tissue segmentation from multispectral MR images," *IEEE Trans. on Medical Imaging*, vol. 13(3), pp. 441–449, 1994.
19. A. N. Tikhonov and V. Y. Arsenin. *Solution of ill-posed problems*. Winston, New York, 1977.
20. I. Cohen, L. Cohen, and N. Ayache. "Using deformable surfaces to segment 3-D images and infer differential structures," *CVGIP: Image Understanding*, vol. 56(2), pp. 242–263, 1992.
21. C. A. Davatzikos and J. L. Prince. "An active contour model for mapping the cortex," *IEEE Trans. on Medical Imaging*, vol. 14(1), pp. 65–80, 1995.
22. N. Rougon and F. Prêteux. "Directional adaptive deformable models for segmentation with application to 2D and 3D medical images," in *SPIE Medical Imaging VII, vol. 1898*, Newport Beach, California, 1993, pp. 193–207.
23. C. N. Lee, T. Poston, and A. Rosenfeld. "Holes and genus of 2D and 3D digital images," *CVGIP: Graph. Models and Image Proc.*, vol. 55(1), pp. 20–47, 1993.
24. W. Hurewicz and H. Wallman. *Dimension theory*. Princeton University Press, Princeton, New Jersey, 1948.
25. R. H. Crowell and R. H. Fox. *Introduction to knot theory*. Blaisdell publishing Company, 1963.
26. V. A. Kovalevsky. "Finite topology as applied to image analysis," *Comput. Vision, Graph. Image Proc.*, vol. 46, pp. 141–161, 1989.
27. G. T. Herman. "On topology as applied to image analysis," *Comput. Vision, Graph. Image Proc.*, vol. 52, pp. 409–415, 1990.
28. G. T. Herman and D. Webster. "A topological proof of a surface tracking algorithm," *Comput. Vision, Graph. Image Proc.*, vol. 23, pp. 162–177, 1983.
29. G. Malandain, G. Bertrand, and N. Ayache. "Topological segmentation of discrete surfaces," *Int. J. of Computer Vision*, vol. 10(2), pp. 158–183, 1993.
30. T. Y. Kong. "A digital fundamental group," *Comput. Graphics*, vol. 13, pp. 159–166, 1989.
31. J. Serra. *Image Analysis and Mathematical Morphology*. Academic Press, 1982.
32. D. G. Morgenthaler. "Three-dimensional simple points: Serial erosion, parallel thinning and skeletonization," *Comput. Vision Laboratory, University of Maryland, Technical Report TR-1005*, 1981.
33. T. Y. Kong and A. Rosenfeld. "Digital topology: Introduction and survey," *Comput. Vision, Graph. Image Proc.*, vol. 48, pp. 357–393, 1989.
34. T. Y. Kong. "On the problem of determining whether a parallel reduction operator for n-dimensional binary images always preserves topology," in *SPIE Vision Geometry II*, vol. 2060, 1993, pp. 69–77.
35. G. Bertrand and G. Malandain. "A new characterisation of three-dimensional simple points," *Pattern Recognition Letters*, vol. 15, pp. 169–175, 1994.
36. G. Bertrand. "Simple points, topological numbers and geodesic neighborhoods in cubic grids," *Pattern Recognition Letters*, vol. 15, pp. 1003–1010, 1994.
37. P. K. Saha and B. B. Chaudhuri. "Detection of 3D simple points for topology preserving transformations with application to thinning," *IEEE Trans. Pattern Anal. Mach. Intell.*, vol. 16(10), pp. 1028–1032, 1994.
38. S. Geman and D. Geman. "Stochastic relaxation, Gibbs distributions and the Bayesian restoration of images," *IEEE Trans. Pattern Anal. Mach. Intell.*, vpl. 6(6), pp. 721–741, 1984.
39. X. Descombes, J.-F. Mangin, E. Pechersky, and M. Sigelle. "Fine structure preserving Markov model for image processing," in *IXth. Scandinavian Conference on Image Analysis*, Uppsala, Sweden, 1995, pp. 349–356.
40. J.-F. Mangin, I. Bloch, J. Lopez-Krahe, and V. Frouin. "Chamfer distances in anisotropic 3D images," in *VIIIth. European Signal Processing Conference*, Edimburgh, Scotland, 1994, pp. 975–978.
41. J.-F. Mangin, F. Tupin, V. Frouin, I. Bloch, R. Rougetet, J. Régis, and J. Lopez-Krahe. "Deformable topological models for segmentation of 3D medical images," in *XIVth. Int. Conf. on Information Processing in Medical Imaging*, France (Kluwer), 1995, pp. 153–164.
42. J. Besag. "Spatial interaction and statistical analysis of lattice systems," *A. Royal Stat. Soc. Serie B*, vol. 36, pp. 721–741, 1976.
43. Y. F. Tsao and K. S. Fu. "A parallel thinning algorithm for 3D pictures," *Comput. Vision, Graph. Image Proc.*, vol. 17, pp. 315–331, 1981.
44. W. X. Gong and G. Bertrand. "A simple parallel 3D thinning algorithm," in *Xth. Int. Conf. on Pattern Recognition*, Atlantic City, USA, 1990, pp. 188–190.
45. R. H. Fox. "On homotopy type and deformation retracts," *Ann. of Math.*, vol. 44, pp. 40–50, 1943.

**Jean-François Mangin** received the engineer degree from École Centrale Paris in 1989, the M.Sc. degree in numerical analysis from Pierre et Marie Curie University (Paris VI) in 1989, and the PhD degree in signal and image processing from École Nationale Supérieure des Télécommunications of Paris in 1995. Since 1991, he has been working with

Service Hospitalier Frédéric Joliot, Commissariat à l'Énergie Atomique, Orsay, France. His research interests include multimodal image registration, pattern recognition, image segmentation, mathematical morphology, Markovian random fields, deformable models, and brain functional mapping.



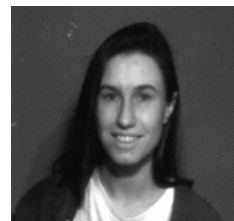
J-F Mangin

**Vincent Frouin** received the engineer degree from École Nationale Supérieure des Télécommunications of Paris in 1987. From 1987 until 1989 he worked with MATRA Velizy France in the R&D group on optical character recognition. Since 1990, he has been working at Service Hospitalier Frédéric Joliot, Commissariat à l'Énergie Atomique, Orsay, France. His research interests include medical functional image analysis (nuclear medicine and functional MRI), multimodal image registration and functional brain mapping.



V. Frouin

**Isabelle Bloch** received the engineer degree from École des Mines de Paris in 1986 and the PhD degree in signal and image processing from École Nationale Supérieure des Télécommunications of Paris in 1990. She is currently associate professor at ENST (Département Images). Her research interests include 3D image and object processing, computational and discrete geometry, 3D and fuzzy mathematical morphology, decision theory, data fusion in image processing, fuzzy set theory, evidence theory, 3D multi-modality medical imaging.



I. Bloch

**Jean Régis** is resident in neurosurgery in Marseille, France, since 1987 and is specialist in stereotactic and functional neurosurgery. In 1994, he received the MD degree from Aix-Marseille II University. He is working in Professor Peragut Neurosurgical Department, CHU La Timone, Marseille where he is specially involved in gamma knife radiosurgery and epilepsy surgery. He published a first report on radiosurgical treatment of temporomesial epilepsy in 1994, which opened a new application field for radiosurgery. Moreover, he has been working on cere-

bral cortex functional anatomy since 1987 which led him to publish a book on pediatric brain development in 1990 with Pr. Salamon and Dr. Raynaud and to propose an original description of cortex gyration for presurgical 3D transsulcal planning.



J. Régis

grees in Psychology as well as in computer Science from Paris VIII University in 1979 and the Ph.D. From Madrid University in 1982. He joined the Image Department of ENST Paris in 1976. His research interests include pattern recognition, computer vision, computational and discrete geometry, image understanding, Hough transform and technological developments for human disability. He is now professor in computer science at Paris VIII University.



J. López-Krahe

**Jaime López-Krahe** was born in Zamora (Spain) in 1946. He received the B.S., M.S. and Ph.D. de-